RSC Advances

PAPER

View Article Online
View Journal | View Issue

Cite this: *RSC Adv.*, 2017, **7**, 36319

In situ fabrication of porous $MnCo_xO_y$ nanocubes on Ti mesh as high performance monolith de-NO_x catalysts†

Jing Xu,‡ Hongrui Li,‡ Yan Liu, Lei Huang, Jianping Zhang, Liyi Shi and Dengsong Zhang*

Herein, we have rationally designed and fabricated porous $MnCo_xO_y$ nanocubes on a Ti mesh *in situ*, as a novel monolith de-NO_x catalyst for selective catalytic reduction of NO by NH_3 (NH_3-SCR). The catalysts were systematically examined by X-ray diffraction, scanning electron microscopy, transmission electron microscopy, elemental mapping and catalytic performance tests. The results indicate that the surface of the titanium mesh is uniformly coated with a layer of cube-like arrays, and each cube is formed by the stacking of regular sheet layers. This structure could prevent the migration and agglomeration of metal oxides and enable the synergistic performance of the components during the catalytic reaction. In addition, due to the robust structure and morphology, the catalyst can sustain high NO conversion, while exhibiting superior catalytic cycle stability and good H_2O resistance. Considering all these favorable properties, the developed material could serve as a promising candidate for monolith de-NO_x catalysts; the *in situ* synthesis of hierarchical monolith catalysts also illustrates a new path for the development of environment-friendly and highly active monolith de-NO_x catalysts.

Received 17th March 2017
Accepted 5th July 2017

DOI: 10.1039/c7ra03182c

rsc.li/rsc-advances

Introduction

Nitrogen oxides (NO_x) are one of the major air pollutants that can cause several ecological problems.[1–3] The selective catalytic reduction of NO by NH_3 (NH_3-SCR) is one of the most efficient techniques for the control of NO_x from stationary and mobile sources.[4–9] Various catalysts that use this technique have been reported. Among them, V_2O_5–WO_3 (MoO_3)/TiO_2 has been widely used commercially. However, there are some inevitable disadvantages during the application, such as the high working temperature, the high conversion of SO_2 to SO_3 and the toxicity of vanadium species to the environment and human health.[10–14] Moreover, the SCR unit is installed upstream of the particle collector and desulfurizer in order to avoid reheating of the flue gas. Therefore, a highly active catalyst for low temperature SCR, which can be placed downstream of the electric precipitator and desulfurizer, is required.[15,16]

It has been demonstrated that Mn-based metal oxides showed an excellent low temperature activity for the SCR reaction.[17–23] Meng *et al.*[24] found that the N_2 selectivity of the Mn–Co mixed-oxide catalyst is higher than those of Co_3O_4 and MnO_x in the temperature range from 50 °C to 375 °C due to the abundant surface acid sites, large active surface oxygen and good redox ability. Thirupathi *et al.*[25] compared a series of Co/Mn atomic ratios and found that NO conversion and the broadening of the temperature window was greatly improved at Co/Mn = 0.4, due to the formation of a two-dimensional monolayer coverage. We[26] developed a catalyst based on hollow porous $Mn_xCo_{3-x}O_4$ nanocages with excellent low-temperature SCR activity, high stability, and H_2O and SO_2 tolerance. This structure had a large surface area and more active sites to adsorb and activate the reaction gases. Moreover, the uniform distribution and strong interaction of manganese and cobalt oxide species strongly enhanced the catalytic cycle and inhibited the formation of manganese sulphate. However, the Mn–Co mixed-oxide catalyst was obtained only as particles. For industrial application, active catalysts are usually supported on monolithic honeycombs by wash-coating. The main drawbacks of these catalysts are nonuniform coating, weight loss, low inter-phase mass transfer rates and low mechanical strength.[27–31] Metal substrates could be alternative choices due to their good thermal and mechanical properties, controllable mass transport, recyclability, and other advantages.[32] Therefore, we have rationally designed and fabricated porous $MnCo_xO_y$ nanocubes on Ti mesh *in situ*, as a novel monolith de-NO_x catalyst for the NH_3-SCR reaction of NO. The synthetic route is schematically illustrated in Scheme 1. TiO_2 contributes a high

Research Center of Nano Science and Technology, School of Material Science and Engineering, Shanghai University, Shanghai 200444, China. E-mail: dszhang@shu.edu.cn; Fax: +86-21-66136079; Tel: +86-21-66137152

† Electronic supplementary information (ESI) available: SEM images of $MnCo_xO_y$@TiO_2@Ti wire mesh prepared with different precursor concentrations; SEM images of $MnCo_xO_y$@TiO_2@Ti wire mesh prepared with different reaction times; effect of NH_3-SCR properties of wire mesh $MnCo_xO_y$@TiO_2@Ti with different quantities of Mn and Co. See DOI: 10.1039/c7ra03182c

‡ These authors contributed equally to this work.

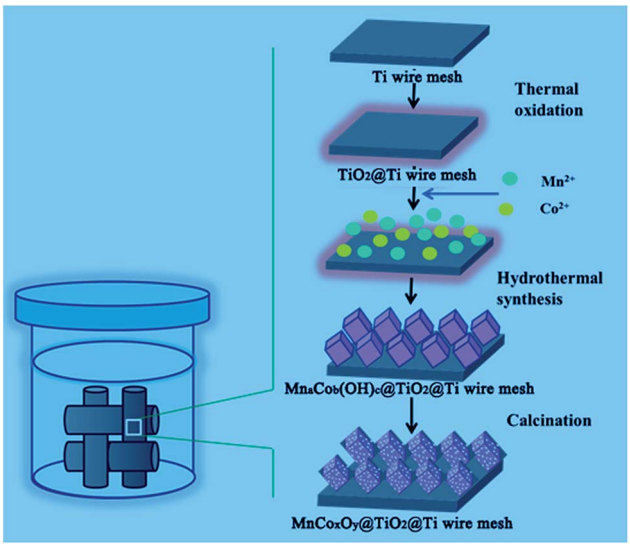

Scheme 1 Schematic of the synthesis of the $MnCo_xO_y$@TiO_2@Ti wire mesh.

surface area, high thermal stability and possesses profound surface acid–base properties to improve the resistance of SO_2.[33–37] Thus, TiO_2 as a good carrier was obtained by the high temperature calcination of Ti mesh. Then, $MnCo_xO_y$ precursor nanocube arrays are obtained by the urea assisted co-precipitation of Mn^{2+} and Co^{2+} nanoparticles on the surface of TiO_2. Finally, the calcination procedure yields the $MnCo_xO_y$@TiO_2@Ti wire mesh. In this design, the $MnCo_xO_y$ nanocubes were anchored on the surface of the Ti wire mesh through TiO_2. This structure could prevent the migration and agglomeration of the metal oxides and enable a synergistic performance between all the components during the catalytic reaction. The $MnCo_xO_y$@TiO_2@Ti wire mesh catalyst can potentially serve as a high performance monolith de-NO_x catalyst.

Experimental

Catalyst preparation

All reagents were of analytical grade, purchased from Sinopharm Chemical Reagent Co. Ltd (China) and used without further purification. The Ti wire mesh was purchased from Anping Kaian Metal Mesh Co. Ltd (Hebei, China). Before use, the Ti wire mesh was cut into pieces (3 cm × 11 cm, $d = 0.8$ cm) and pretreated with 4 M HNO_3 aqueous solution at 60 °C for 4 h. Then, the Ti wire mesh was washed by isopropanol upon ultrasonication for 20 min, to remove the dirt and grease, and finally dried at 60 °C in the oven.

In a typical synthesis, the Ti wire mesh was treated at 600 °C for 4 h with a ramping rate of 2 °C min^{-1} in air. A series of $MnSO_4 \cdot H_2O$, $Co(NO_3)_2 \cdot 6H_2O$ and 24 mmol of urea were dissolved in 80 mL of deionized water under stirring for 1 h. Subsequently, the pretreated Ti wire mesh was immersed in the above-mentioned homogeneous solution and transferred to a 100 mL Teflon-lined stainless steel autoclave. The autoclave was heated and maintained at 90 °C for 24 h and then allowed to cool to room temperature naturally. The Ti wire mesh was washed by deionized water, dried overnight at 60 °C, and finally calcined in air at 600 °C for 4 h with a ramping rate of 1 °C min^{-1}.

The $MnCo_xO_y$/TiO_2/honeycomb ceramics and V–W/TiO_2/honeycomb ceramics as reference samples were also fabricated *via* similar procedures. The preparation of the $MnCo_xO_y$/TiO_2/honeycomb ceramics catalyst was carried out as follows. The commercial cordierite ceramic honeycomb (400 cells per square inch, 1 mm^2 square channels and 100 μm a wall thickness) was purchased from the Yixing Weimin Ceramics Factory (China) and cut into a cylinder with a diameter of 2 cm and a height of 3 cm. The cordierite was pre-treated with ethanol and deionized water and dried at 70 °C overnight. According to the loadings of active component $MnCo_2O_4$ on TiO_2 wire mesh (the mass difference before and after the reaction), 0.087 g of $MnSO_4 \cdot H_2O$ and 0.302 g of $Co(NO_3)_2 \cdot 6H_2O$ were dispersed in 10 mL deionized water under stirring for 20 min. Then, the pre-treated cordierite ceramic honeycomb was repeatedly immersed in the homogeneous solution and dried at 80 °C, until the active component entirely covered the cordierite. Finally, the products were calcined in air at 450 °C for 4 h at a ramping rate of 5 °C min^{-1}.

The V–W/TiO_2/honeycomb ceramics catalyst was obtained by a similar process as described above, except that the active component was obtained from 0.00257 g NH_4VO_3, 0.02187 g $(NH_4)_{10}W_{12}O_{41} \cdot xH_2O$ and 0.178 g TiO_2.

Characterization

The morphology and elemental information of the as-synthesized samples were monitored by a scanning electron microscope (SEM, JEOL JSM-6700F) equipped with an energy dispersive X-ray spectrometry (EDX) system. The samples were deposited on a sample holder with a piece of adhesive carbon tape and sputtered with a thin film of gold. Powder X-ray diffraction (XRD) patterns were recorded on a Rigaku D/MAX-RB X-ray diffractometer with Cu Kα (40 kV, 40 mA) radiation and a secondary beam graphite monochromator.

Catalytic tests

The SCR experiments were carried out at atmospheric pressure in a fixed-bed stainless steel flow reactor (i.d. 1 cm). The temperature of the reactor was monitored and controlled by thermocouples that were inserted into the centre of the catalyst bed. The reactant gases were fed to the reactor by an electronic mass flow controller. The typical reactant gas composition was as follows: 500 ppm NO, 500 ppm NH_3, 3 vol% O_2 and N_2 as balance. The NO-SCR experiments were performed over the catalysts from 100 to 470 °C and the gas hourly space velocity (GHSV) was 10 000 h^{-1}. The inlet and outlet concentrations of NO from the reactor were analyzed by a NO–NO_x analyzer (KM9106). The concentrations of N_2O and NH_3 were measured by a transmitter IR N_2O analyzer and IQ350 ammonia analyzer, respectively. All the stream lines were maintained at approximately 110 °C to prevent condensation of water and

dissolution of NH_3 in water. The NO conversion was calculated according to the following equation:

$$\text{NO conversion } (\%) = \frac{[\text{NO}]_{\text{in}} - [\text{NO}]_{\text{out}}}{[\text{NO}]_{\text{in}}} \times 100\%$$

where $[\text{NO}]_{\text{in}}$ and $[\text{NO}]_{\text{out}}$ indicated the inlet and outlet concentrations at steady-state, respectively.

Results and discussion

Morphology and structure of the catalysts

The morphology and structure of the $MnCo_xO_y$@TiO_2@Ti wire mesh were studied by SEM and TEM. Fig. 1 shows the SEM images of the $MnCo_xO_y$@TiO_2@Ti wire mesh. Manganese and cobalt ions are deposited on the surface of the titanium mesh *in situ* by a hydrothermal reaction to form precursor salts and yield a uniform coating of the manganese and cobalt composite oxide layer upon calcination. The active component oxides closely combined with the metal wire mesh carrier are beneficial for the effective mass transfer and heat transfer in the process of denitrification, which can avoid the effect of catalyst sintering.[34,38] The surface of the titanium mesh is uniformly coated with a layer of a cube arrays, and each cube is formed by the stacking of regular sheet layers (Fig. 1b and c). The cube layer is composed of uniform particles (Fig. 1d), which is due to the decomposition of cubic precursor salts. Several inorganic species (H_2O, NO_2, SO_2, *etc.*) volatilize by decomposition and diffuse to form the ordered pores. The cubes could not be obtained without the Ti wire mesh (Fig. S1†). The three-dimensional hierarchical structure not only has a larger effective specific surface area, which helps to expose more reactive sites and adsorb more reactive gas molecules, but also avoids the sintering of the active component at high temperature. The manganese cobalt compound oxides can play a synergistic catalytic role on the improved performance of the monolith catalysts.

Fig. 2 shows the TEM images of $MnCo_xO_y$ (the active components were scraped off from the titanium mesh surface).

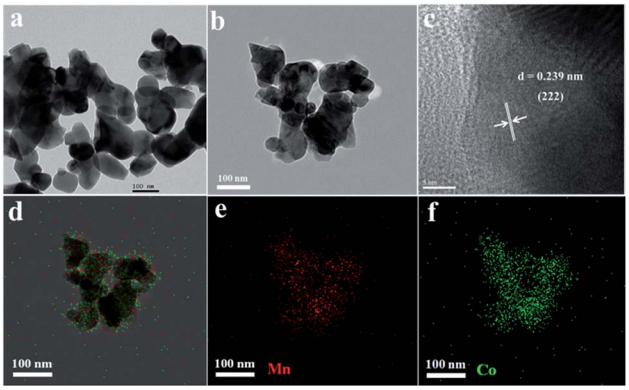

Fig. 2 (a) TEM, (b) STEM, (c) HRTEM, and (d–f) EDX-mapping images of the $MnCo_xO_y$@TiO_2@Ti wire mesh.

The obtained $MnCo_xO_y$ nanoparticles are uniform with an average size of 80–120 nm (Fig. 2a and b). The HRTEM image of $MnCo_xO_y$ (Fig. 2c) showed lattice fringes in the (222) direction with an interplanar spacing of 0.239 nm. In order to understand the surface elemental distribution of $MnCo_xO_y$@TiO_2@Ti, the EDX-mapping is shown in Fig. 2d–f. The Mn and Co elements show a highly uniform distribution in the $MnCo_xO_y$ nanoparticles, indicating that the Mn and Co atoms are arranged in the cube-like structure and have a strong interaction between them.[26] This structure ensures the uniform dispersion of the active components to improve the catalytic activity.

The XRD patterns of the $MnCo_xO_y$ powders scraped from the Ti wire mesh also confirm the formation of $MnCo_xO_y$ (Fig. 3); the peaks at 18.55°, 30.54°, 35.99°, 43.76°, 54.34°, 57.91°, 63.62° and 76.35° indicate that the nanocrystals of $MnCo_2O_4$ possess the spinel structure (JCPDS 23-1237). The diffraction peaks are narrow and strong, which means that the $MnCo_2O_4$ has small particle size and regular morphology. This is also consistent with the results of SEM and TEM.

The chemical states on the catalyst surface were investigated by XPS measurements. The catalyst shows two overlapping peaks of the O 1s (Fig. S2a†); the low binding energy peak

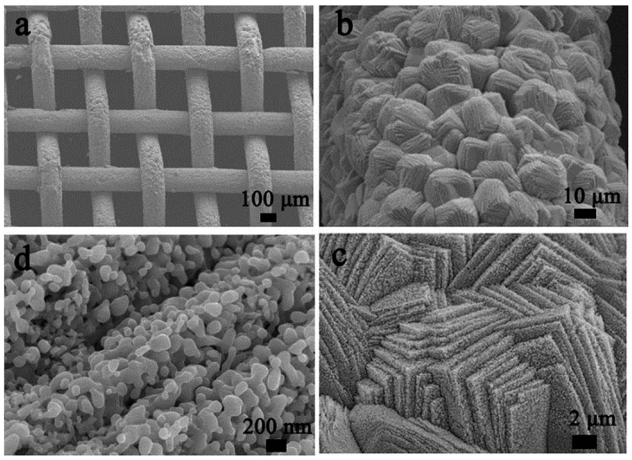

Fig. 1 SEM images of the $MnCo_xO_y$@TiO_2@Ti wire mesh. (a) Overview; (b) surface morphology of wires; (c) morphology of cubic layers; and (d) microstructure of cubic layers.

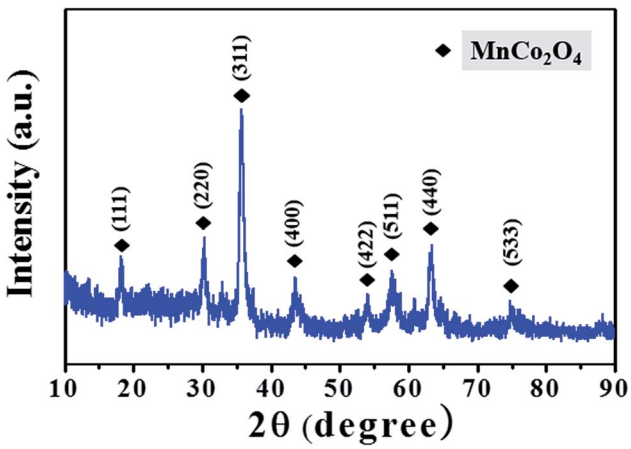

Fig. 3 XRD patterns of the $MnCo_xO_y$ powders scraped from the Ti wire mesh.

(531.8 eV) was assigned to lattice oxygen, and the high binding energy peak (533.0 eV) was attributed to chemisorbed oxygen, which could originate from defect oxides or hydroxyl-like groups. The surface chemisorbed oxygen has been reported as the most active oxygen, particularly in the oxidation reaction due to its higher mobility. The abundance of chemisorbed oxygen in $MnCo_xO_y$@TiO_2@Ti wire mesh may enhance the NH_3-SCR reaction by participating in the "fast SCR" reaction route.

The Co $2p_{3/2}$ spectrum of the catalyst is fitted into two peaks assigned to Co^{3+} (779.9 eV) and Co^{2+} (781.5 eV) (Fig. S2b†). The Co^{3+} species is preferred for the oxidation cycle among the various valence states of cobalt, resulting in an enhancement of NH_3 chemisorption. Thus, the Co^{3+} species could enhance the catalytic activity.

The Mn $2p_{3/2}$ spectra can be divided into three characteristic peaks attributed to Mn^{2+} (640.6 eV), Mn^{3+} (642.0 eV), and Mn^{4+} (644.1 eV) (Fig. S2c†). The Mn^{4+} species and its redox cycle might contribute to the high activity in the NH_3-SCR reaction at low temperatures and enhance oxidation of NO to NO_2.

The H_2-TPR analysis was employed to evaluate the reducibility of the catalyst. The TPR profiles of the $MnCo_xO_y$@TiO_2@Ti wire mesh are shown in Fig. S3.† As can be seen, the catalyst shows three distinct peaks at 306, 406, and 457 °C. The low temperature peak at 306 °C corresponds to the reduction of the manganese species. The later peaks at 406 and 457 °C are attributed to the Co^{3+} to Co^{2+} and Co^{2+} to Co^0 transitions, respectively.

The NH_3-TPD experiments were performed to investigate the adsorption and activation of NH_3 on the surface acid sites of the catalyst, which is generally viewed as the key process in the NH_3-SCR of NO. In the NH_3-TPD profile (Fig. S4†), the low temperature desorption peaks between 100 and 300 °C belong to the ammonia desorbed from weak Lewis or Brønsted acid sites and the high temperature desorption peaks between 300 and 600 °C belong to the ammonia desorbed from strong acid sites.[3] Therefore, the NH_3-TPD measurement was performed as shown in Fig. S4.† The catalyst exhibits two desorption peaks: the weak peak centred at 190 °C attributed to ammonia desorbed from the weak acid sites, and the strong peak observed at 484 °C assigned to ammonia desorbed from the strong acid sites on the catalyst. This reveals a much larger area, indicating the presence of several acid sites.

Catalytic performance

The NH_3-SCR activity of $MnCo_xO_y$@TiO_2@Ti wire mesh is shown in Fig. 4. For comparison, manganese salt, cobalt salt and TiO_2 were impregnated on the conventional honeycomb ceramics and the V–W/TiO_2/honeycomb ceramics catalyst was also prepared. The $MnCo_xO_y$@TiO_2@Ti wire mesh and $MnCo_xO_y$/TiO_2/honeycomb ceramics show a similar NO conversion, implying that the Mn and Co mixed oxides are the active components. In the range of 200–425 °C, the $MnCo_xO_y$@TiO_2@Ti wire mesh shows a better NO conversion than the $MnCo_xO_y$/TiO_2/honeycomb ceramics. Particularly, at 275–350 °C, the maximum NO conversion of the $MnCo_xO_y$@TiO_2@Ti wire mesh is 95%, and 92% for the $MnCo_xO_y$/TiO_2/honeycomb ceramics. During the five recyclable

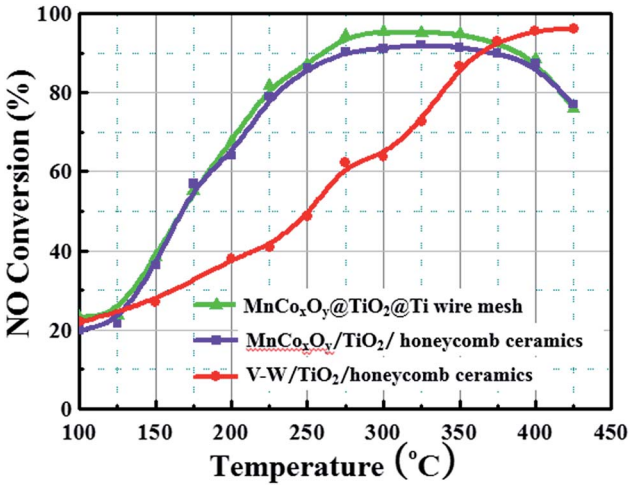

Fig. 4 NH_3-SCR performance of the $MnCo_xO_y$@TiO_2@Ti wire mesh, $MnCo_2O_4$/honeycomb ceramics and V–W–T/honeycomb ceramics as a function of temperature. Conditions: [NO] = [NH_3] = 500 ppm, [O_2] = 3 vol%, N_2 as balance gas, and GHSV = 10 000 h^{-1}.

catalytic tests, the maximum NO conversion remains at 95% (Fig. S5†). The three-dimensional titanium wire mesh support is more favourable for improved denitrification performance compared to traditional ceramic honeycomb carriers due to its good mechanical properties and heat transfer performance. This can also avoid the sintering of the active component of the catalyst at high temperature and influence the catalytic performance. Additionally, the metal wire mesh are easier to recycle as compared to the ceramic. From Fig. 4, the V–W/TiO_2/honeycomb ceramics show a maximum NO conversion of 97% at 400 °C. Thus, the $MnCo_xO_y$@TiO_2@Ti wire mesh and $MnCo_xO_y$/TiO_2/honeycomb ceramics display denitrification activity at lower temperatures than the V–W/TiO_2/honeycomb ceramics, which further confirms that these catalysts with the active components of cobalt manganese composite oxides are conducive to practical application. Therefore, the titanium wire mesh is demonstrated as an excellent catalyst substrate for the removal of NO_x, which is expected to replace the traditional honeycomb ceramic carrier. In addition, it can be recycled to avoid environmental pollution and wastage of resources. A comparison of the $MnCo_xO_y$@TiO_2@Ti wire mesh with other high-activity Mn-based catalysts that were reported in the literature has been summarized in Table S1.† Thus, Mn or Mn–Co is a good de-NO_x catalyst, but those are powders rather than monolith.

A relative turnover frequency (TOF) value was employed to calculate the activities of the catalyst. The relative TOF (s^{-1}) of NO over each Mn atom was calculated by the following equation:

$$\mathrm{TOF} = \frac{\left(\frac{P\upsilon}{RT}\right)\alpha}{\frac{m_{\mathrm{cat}}\beta_{\mathrm{Mn}}}{M_{\mathrm{Mn}}}}$$

where P is the standard atmospheric pressure (1.01×10^5 Pa); υ is the flow rate of NO (1.0 mL min^{-1}); R is the proportional constant (8.314 J mol^{-1} K^{-1}); T is the room temperature (298 K); α is the NO conversion of the catalyst (%); m_{cat} is the mass of the

catalyst; β_{Mn} is the Mn loading calculated from the XPS spectra (%) and M_{Mn} is the molar mass of Mn (54.94 g mol^{-1}). Based on the NO conversion at 150 °C, the TOF for the $MnCo_xO_y$@TiO_2@Ti wire mesh, calculated using the above equation, was 2.7×10^{-3} s^{-1}.

In order to have a better understanding of the improved morphology and catalytic ability of the $MnCo_xO_y$@TiO_2@Ti wire mesh, different conditions were investigated. With a change in solution concentration, the obtained morphology is different (Fig. S6†). When the molar amount of Mn is 4 mmol, the highest loading of the surface active component on the titanium wire mesh is observed, the layered cubic structure is the most regular and displays the most exposed surface, which enables adsorption and activation of the gas molecules in the process of denitrification and improves the catalyst activity. With the increase of duration of the hydrothermal reaction, the active load gradually increased and an even load was obtained on the surface (Fig. S7†). The saturated load was achieved at 12 h and did not display a significant change upon further increase of the duration.

There is a close relationship between the activity of the monolith catalyst and the proportion of the components. Different proportions of the monolith catalyst may have different crystal structures, specific surface areas and redox properties, which ultimately lead to different catalyst activities.[39–47] When the concentration of $MnSO_4 \cdot H_2O$ was 4 mmol and Co $(NO_3)_2 \cdot 6H_2O$ was 8 mmol, the monolith catalyst exhibited the best catalytic activity in the entire temperature range, compared to the other catalysts (Fig. S8†). In the temperature range 275–400 °C, the NO conversion rate is more than 87% and reached a maximum value of 96% at 325 °C.

The NO conversion under different GHSVs is very crucial for practical applications.[6,28] Fig. 5 shows the NO conversion of $MnCo_2O_4$ under different space velocities. At 10 000 h^{-1}, the catalyst displayed the best performance. In the range 200–400 °C, the NO conversion was >70%, while it was >94% at 275–350 °C. At 20 000 h^{-1}, the NO conversion was 90% at 325 °C and reduced at all other temperatures. The entire catalytic activity window became narrow. At 30 000 h^{-1}, the catalytic activity decreased significantly and the maximum conversion rate of NO was 74%. The entire active range window shifted to the high temperature zone. The results show that the denitrification activity of the $MnCo_xO_y$@TiO_2@Ti wire mesh decreased gradually with the increase in space velocity. From the actual operating temperature range and the maximum NO conversion requirements, the appropriate gas flow rate or amount of catalyst to achieve the corresponding space velocity condition can be selected.

The catalytic stability is quite important in practical applications for the catalyst. Fig. 6 shows the stability test curve of the $MnCo_xO_y$@TiO_2@Ti wire mesh at 325 °C. In the first 2 h, NO conversion significantly decreased from 98% to 95% and slowly reduced further to 92% after a long test of 13 h. Thus, the NO conversion was maintained at >90% during the entire test. This shows that the $MnCo_xO_y$@TiO_2@Ti wire mesh can not only provide high NH_3-SCR activity in a wide range of operating temperatures, but can also maintain a high NO conversion rate under longer test conditions. This also proves that the mechanical stability and the three dimensional structure of the catalyst support titanium mesh enables a good mass transfer and heat transfer performance to avoid the sintering of the catalyst in the long term test. The stability of the $MnCo_xO_y$/TiO_2/honeycomb and V–W/TiO_2/honey-comb ceramics was also tested (Fig. S9†). The result of $MnCo_xO_y$/TiO_2/honeycomb ceramics is similar to that of the $MnCo_xO_y$@TiO_2@Ti wire mesh, but the NO conversion is lower due to the aggregation of nanoparticles and poor transformation. The NO conversion of V–W/TiO_2/honeycomb ceramics is relatively low and descends rapidly.

Some residual H_2O always exists in the exhaust fume, which can deactivate the catalyst if adsorbed on the active sites.[39–42] The test curve of the $MnCo_xO_y$@TiO_2@Ti wire mesh in the presence of 10 vol% water vapor at 325 °C is shown in Fig. 6a. The NO conversion of the catalyst was about 93% in the absence of steam. After the introduction of 10 vol% H_2O, the conversion

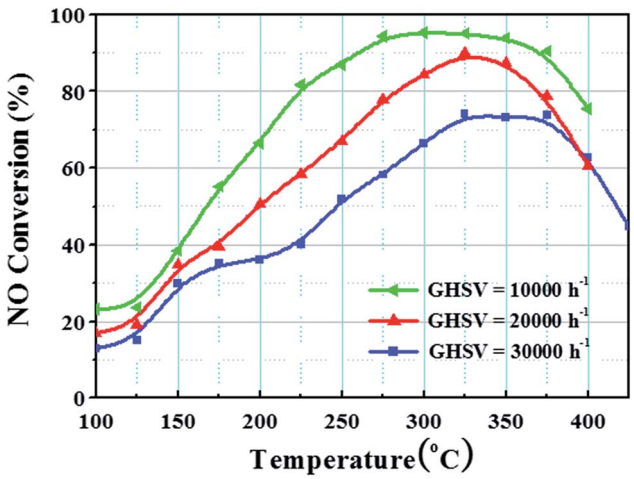

Fig. 5 NH_3-SCR activity of the $MnCo_xO_y$@TiO_2@Ti wire mesh for different GHSVs.

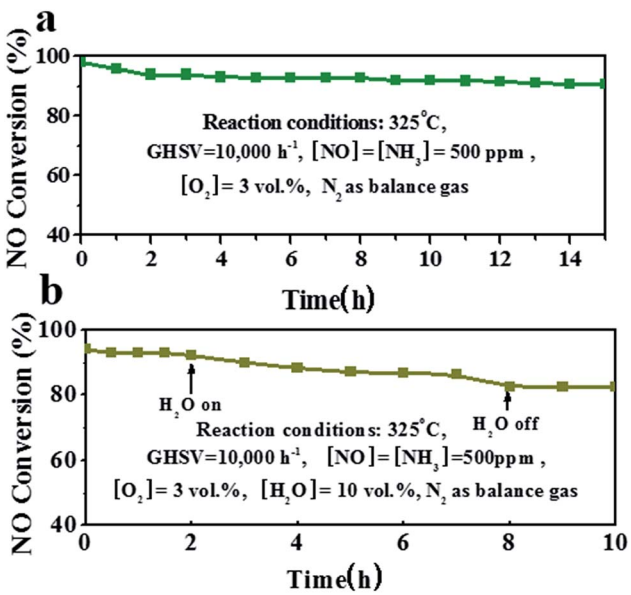

Fig. 6 (a) Stability test at 325 °C for 15 h and (b) H_2O durability test of the $MnCo_xO_y$@TiO_2@Ti wire mesh at 325 °C.

rate slowed to 89% during the 6 h test. This is because the water vapor and NH_3 molecules on the surface of the catalyst compete for adsorption sites to inhibit the adsorption and activation of reactive gas molecules. However, after removing H_2O, the conversion of NO remained unchanged. The NO conversion of the catalyst was >90% during the entire process of water resistance testing, which shows that the catalyst has better ability to resist H_2O steam toxicity. The performance of H_2O resistance at 275 °C is similar (Fig. S10†). After the introduction of 10 vol% H_2O, the conversion rate slows to 80% during the 6 h test.

Conclusions

In summary, we have rationally designed and fabricated porous $MnCo_xO_y$ nanocubes on Ti mesh *in situ* as a novel monolith de-NO_x catalyst for NH_3-SCR of NO. The $MnCo_xO_y$@TiO_2@Ti wire mesh catalyst displays an enhanced NH_3-SCR activity compared to the honeycomb ceramics based monolith catalysts, with a maximum NO conversion of 95% at 275 °C. The NO conversion is maintained >90% at a GHSV of 10 000 h^{-1} within the broad temperature window from 275 °C to 400 °C. The surface of the titanium mesh is uniformly coated with a layer of cube-like arrays, and each cube is formed by the stacking of regular sheet layers. This structure could prevent the migration and agglomeration of metal oxides and provide a synergistic performance between the components during the catalytic reaction. The catalyst can sustain high NO conversion and exhibits superior catalytic cycle stability and good H_2O resistance. The *in situ* growth of composite metal oxides on the wire mesh can not only reduce environmental pollution due to the binder in the traditional monolithic catalyst, but also can be easily recovered twice. The wire mesh has good mechanical and mass transfer properties, which benefits the denitrification reaction. The idea and the concept of the preparation of the novel monolithic de-NO_x catalyst are of great significance for the development and design of new monolithic catalysts.

Acknowledgements

The authors acknowledge the support of the National Natural Science Foundation of China (U1462110).

Notes and references

1 M. F. Fu, C. T. Li, P. Lu, L. Qu, M. Y. Zhang, Y. Zhou, M. G. Yu and Y. Fang, *Catal. Sci. Technol.*, 2014, **4**, 14–25.
2 P. Zhang and D. Y. Li, *Catal. Lett.*, 2014, **144**, 959–963.
3 T. Zhang, J. Liu, D. Wang, Z. Zhao, Y. Wei, K. Cheng, G. Jiang and A. Duan, *Appl. Catal., B*, 2014, **148**, 520–531.
4 S. J. Yang, F. H. Qi, Y. Liao, S. C. Xiong, Y. Lan, Y. W. Fu, W. P. Shan and J. H. Li, *Ind. Eng. Chem. Res.*, 2014, **53**, 5810–5819.
5 L. J. Xie, F. D. Liu, L. M. Ren, X. Y. Shi, F. S. Xiao and H. He, *Environ. Sci. Technol.*, 2014, **48**, 566–572.
6 Y. Shu, T. Aikebaier, X. Quan, S. Chen and H. T. Yu, *Appl. Catal., B*, 2014, **150**, 630–635.
7 M. S. Maqbool, A. K. Pullur and H. P. Ha, *Appl. Catal., B*, 2014, **152**, 28–37.
8 R. B. Jin, Y. Liu, Y. Wang, W. L. Cen, Z. B. Wu, H. Q. Wang and X. L. Weng, *Appl. Catal., B*, 2014, **148**, 582–588.
9 R. Camposeco, S. Castillo, V. Mugica, I. Mejia-Centeno and J. Marin, *Catal. Commun.*, 2014, **45**, 54–58.
10 S. J. Yang, C. Z. Wang, L. Ma, Y. Peng, Z. Qu, N. Q. Yan, J. H. Chen, H. Z. Chang and J. H. Li, *Catal. Sci. Technol.*, 2013, **3**, 161–168.
11 I. Nova, L. Lietti, L. Casagrande, L. Dall'Acqua, E. Giamello and P. Forzatti, *Appl. Catal., B*, 1998, **17**, 245–258.
12 W. Q. Xu, H. He and Y. B. Yu, *J. Phys. Chem. C*, 2009, **113**, 4426–4432.
13 L. Chen, Z. Si, X. Wu and D. Weng, *ACS Appl. Mater. Interfaces*, 2014, **6**, 8134–8145.
14 Y. Peng, C. X. Liu, X. Y. Zhang and J. H. Li, *Appl. Catal., B*, 2013, **140**, 276–282.
15 S. L. Zhang, X. X. Liu, Q. Zhong and Y. Yao, *Catal. Commun.*, 2012, **25**, 7–11.
16 Y. J. Kim, H. J. Kwon, I. S. Nam, J. W. Choung, J. K. Kil, H. J. Kim, M. S. Cha and G. K. Yeo, *Catal. Today*, 2010, **151**, 244–250.
17 Q. Q. Tian, H. F. Liu, W. Y. Yao, Y. Wang, Y. Liu, Z. B. Wu, H. Q. Wang and X. L. Weng, *J. Nanomater.*, 2014, **4**, 1–6.
18 K. H. Park, S. M. Lee, S. S. Kim, D. W. Kwon and S. C. Hong, *Catal. Lett.*, 2013, **143**, 246–253.
19 S. J. Yang, Y. W. Fu, Y. Liao, S. C. Xiong, Z. Qu, N. Q. Yan and J. H. Li, *Catal. Sci. Technol.*, 2014, **4**, 224–232.
20 C. Tang, H. Zhang and L. Dong, *Catal. Sci. Technol.*, 2016, **6**, 1248–1264.
21 S. Wu, X. Yao, L. Zhang, Y. Cao, W. Zou, L. Li, K. Ma, C. Tang, F. Gao and L. Dong, *Chem. Commun.*, 2015, **51**, 3470–3473.
22 K. Ma, W. Zou, L. Zhang, L. Li, S. Yu, C. Tang, F. Gao and L. Dong, *RSC Adv.*, 2017, **7**, 5989–5999.
23 R.-t. Guo, M.-y. Li, P. Sun, S.-m. Liu, S.-x. Wang, W.-g. Pan, S.-w. Liu, J. Liu and X. Sun, *RSC Adv.*, 2017, **7**, 19912–19923.
24 B. Meng, Z. B. Zhao, Y. S. Chen, X. Z. Wang, Y. Li and J. S. Qiu, *Chem. Commun.*, 2014, **50**, 12396–12399.
25 B. Thirupathi and P. G. Smirniotis, *Appl. Catal., B*, 2011, **110**, 195–206.
26 L. Zhang, L. Shi, L. Huang, J. Zhang, R. Gao and D. Zhang, *ACS Catal.*, 2014, **4**, 1753–1763.
27 Y. Shu, T. Aikebaier, X. Quan, S. Chen and H. Yu, *Appl. Catal., B*, 2014, **150**, 630–635.
28 J. Yao, J. S. Choi, K. S. Yang, D. Z. Sun and J. S. Chung, *Korean J. Chem. Eng.*, 2006, **23**, 888–895.
29 S. Cai, D. Zhang, L. Shi, J. Xu, L. Zhang, L. Huang, H. Li and J. Zhang, *Nanoscale*, 2014, **6**, 7346–7353.
30 L. del Rio and G. Marban, *Appl. Catal., B*, 2012, **126**, 39–46.
31 Z. G. Lei, C. P. Wen, J. Zhang and B. H. Chen, *Ind. Eng. Chem. Res.*, 2011, **50**, 5942–5951.
32 S. Cai, J. Liu, K. Zha, H. Li, L. Shi and D. Zhang, *Nanoscale*, 2017, **9**, 5648–5657.
33 Q. J. Jin, Y. S. Shen and S. M. Zhu, *J. Colloid Interface Sci.*, 2017, **487**, 401–409.

34 Y. Y. He, M. E. Ford, M. H. Zhu, Q. C. Liu, U. Tumuluri, Z. L. Wu and I. E. Wachs, *Appl. Catal., B*, 2016, **193**, 141–150.
35 X. S. Du, X. M. Wang, Y. R. Chen, X. Gao and L. Zhang, *J. Ind. Eng. Chem.*, 2016, **36**, 271–278.
36 F. Giraud, C. Geantet, N. Guilhaume, S. Loridant, S. Gros, L. Porcheron, M. Kanniche and D. Bianchi, *J. Phys. Chem. C*, 2015, **119**, 15401–15413.
37 J. Liu, X. Li, Q. Zhao, J. Ke, H. Xiao, X. Lv, S. Liu, M. Tadé and S. Wang, *Appl. Catal., B*, 2017, **200**, 297–308.
38 H. Li, D. Zhang, P. Maitarad, L. Shi, R. Gao, J. Zhang and W. Cao, *Chem. Commun.*, 2012, **48**, 10645–10647.
39 C. Fang, D. Zhang, L. Shi, R. Gao, H. Li, L. Ye and J. Zhang, *Catal. Sci. Technol.*, 2013, **3**, 803–811.
40 C. Fang, D. Zhang, S. Cai, L. Zhang, L. Huang, H. Li, P. Maitarad, L. Shi, R. Gao and J. Zhang, *Nanoscale*, 2013, **5**, 9199–9207.
41 S. Cai, D. Zhang, L. Zhang, L. Huang, H. Li, R. Gao, L. Shi and J. Zhang, *Catal. Sci. Technol.*, 2014, **4**, 93–101.
42 L. Zhang, D. S. Zhang, J. P. Zhang, S. X. Cai, C. Fang, L. Huang, H. R. Li, R. H. Gao and L. Y. Shi, *Nanoscale*, 2013, **5**, 9821–9829.
43 L. Ma, J. H. Li, R. Ke and L. X. Fu, *J. Phys. Chem. C*, 2011, **115**, 7603–7612.
44 X. A. Gao, X. S. Du, L. W. Cui, Y. C. Fu, Z. Y. Luo and K. F. Cen, *Catal. Commun.*, 2010, **12**, 255–258.
45 M. Casapu, O. Krocher, M. Mehring, M. Nachtegaal, C. Borca, M. Harfouche and D. Grolimund, *J. Phys. Chem. C*, 2010, **114**, 9791–9801.
46 M. Kang, E. D. Park, J. M. Kim and J. E. Yie, *Catal. Today*, 2006, **111**, 236–241.
47 Y. Shu, H. Sun, X. Quan and S. Chen, *J. Phys. Chem. C*, 2012, **116**, 25319–25327.